Time-Domain Reconstruction for Thermoacoustic Tomography in a Spherical Geometry

Minghua Xu and Lihong V. Wang*

Abstract—**Reconstruction-based microwave-induced thermoacoustic tomography in a spherical configuration is presented. Thermoacoustic waves from biological tissue samples excited by microwave pulses are measured by a wide-band unfocused ultrasonic transducer, which is set on a spherical surface enclosing the sample. Sufficient data are acquired from different directions to reconstruct the microwave absorption distribution. An exact reconstruction solution is derived and approximated to a modified backprojection algorithm. Experiments demonstrate that the reconstructed images agree well with the original samples. The spatial resolution of the system reaches 0.5 mm.**

Index Terms—**Microwave, reconstruction, thermoacoustic, tomography.**

I. INTRODUCTION

PULSED-MICROWAVE-INDUCED thermoacoustic tomography in biological tissues combines the advantages of pure microwave imaging [1]–[3] and pure ultrasound imaging [4], [5]. The wide range of microwave absorption coefficients found in different kinds of tissue leads to a high imaging contrast for biological tissues. However, it is difficult to achieve good spatial resolution in biological tissues using pure microwave imaging because of the long wavelength of microwaves. This problem can be overcome by the use of microwave-induced thermoacoustic waves. Because the velocity of acoustic waves in soft tissue is $\sim$1.5 mm/μs, thermoacoustic signals at megahertz can provide millimeter or better spatial resolution.

In thermoacoustic tomography, a short-pulsed microwave source is used to irradiate the tissue. The relatively long wavelength of the microwave, e.g., $\sim$3 cm at 3 GHz in tissues, serves to illuminate the tissue homogeneously. A wide-band ultrasonic transducer can then be employed to acquire the thermoacoustic signals excited by thermoelastic expansion, which carries the microwave absorption property of the tissue.

M. Xu is with the Optical Imaging Laboratory, Department of Biomedical Engineering, Texas A&M University, 3120 TAMU, College Station, TX 77843-3120 USA.

*L. V. Wang is with the Optical Imaging Laboratory, Department of Biomedical Engineering, Texas A&M University, College Station, TX 77843-3120 USA (e-mail: LWang@tamu.edu).

The ultrasonic transducer is very sensitive in detecting small thermoacoustic vibrations from an object.

The key problem with this technique is how to determine the microwave absorption distribution from the measured data, i.e., how to map the inhomogeneity of the tissue. One approach is to use focused ultrasonic transducers to localize the thermoacoustic sources in linear or sector scans and then construct the images directly from the data as is often done in pulse-echo ultrasonography [6], [7]. An alternative method is to use wide-band point detectors to acquire thermoacoustic data and then reconstruct the microwave absorption distribution. To date, we have not seen an exact inverse solution for this specific problem, although some researchers have arrived at approximate reconstruction algorithms, such as the weighted delay-and-sum method [8], the optimal statistical approach [9], and other approach [10].

Based on spherical harmonic functions, in this paper we first deduce an exact solution to the problem in three-dimensional spherical geometry, which can be carried out in the frequency domain [11]–[14]. The exact reconstruction algorithms in planar and cylindrical geometries are reported in the companion papers [15], [16]. Spherical measurement geometry may be more suitable for investigation of external organs such as the breast. We assume that the wide-band unfocused ultrasonic transducer is set on a spherical surface, which encloses the sample under investigation. The data acquired from different directions are sufficient to allow us to reconstruct the microwave absorption distribution.

In many cases, the diameter of the sphere of detection is much larger than the ultrasonic wavelength. As a result, an approximate algorithm can be deduced, which is a modified backprojection of a quantity related to the thermoacoustic pressure. This approximate algorithm can be carried out in the time domain and is much faster than the exact solution. In our initial investigations, we have also tested tissue samples in a circular measurement configuration. These experiments demonstrate that the images calculated by the modified backprojection method agree well with the original samples. Moreover, the images have both the high contrast associated with pure microwave imaging and the 0.5-mm spatial resolution associated with pure ultrasonic imaging.

II. THEORY

A. Fundamental of Thermoacoustics

Thermoacoustic theory has been discussed in many literature reviews such as [13]. Here, we briefly review only the fundamental equations. If the microwave pumping pulse duration is

much shorter than the thermal diffusion time, thermal diffusion can be neglected; consequently, the thermal equation becomes

$$\rho C_P \frac{\partial}{\partial t} T(\mathbf{r}, t) = H(\mathbf{r}, t) \qquad (1)$$

where ρ is the density; C_p is the specific heat; $T(\mathbf{r}, t)$ is the temperature rise due to the energy pumping pulse; and $H(\mathbf{r}, t)$ is the heating function defined as the thermal energy per time and volume deposited by the energy source. We are initially interested in tissue with inhomogeneous microwave absorption but a relatively homogeneous acoustic property. The two basic acoustic generation equations in an acoustically homogeneous medium are the linear inviscid force equation

$$\rho \frac{\partial^2}{\partial t^2} \mathbf{u}(\mathbf{r}, t) = -\nabla p(\mathbf{r}, t) \qquad (2)$$

and the expansion equation

$$\nabla \cdot \mathbf{u}(\mathbf{r}, t) = -\frac{p(\mathbf{r}, t)}{\rho c^2} + \beta T(\mathbf{r}, t) \qquad (3)$$

where β is the isobaric volume expansion coefficient; c is the sound speed; $\mathbf{u}(\mathbf{r}, t)$ is the acoustic displacement; and $p(\mathbf{r}, t)$ is the acoustic pressure.

Combining (1)–(3), the pressure $p(\mathbf{r}, t)$ produced by the heat source $H(\mathbf{r}, t)$ obeys the following equation:

$$\nabla^2 p(\mathbf{r}, t) - \frac{1}{c^2} \frac{\partial^2}{\partial t^2} p(\mathbf{r}, t) = -\frac{\beta}{C_p} \frac{\partial}{\partial t} H(\mathbf{r}, t). \qquad (4)$$

The solution based on Green's function can be found in the literature of physics or mathematics [12], [14]. A general form can be expressed as

$$p(\mathbf{r}, t) = \frac{\beta}{4\pi C_p} \iiint \frac{d^3 r'}{|\mathbf{r} - \mathbf{r}'|} \left. \frac{\partial H(\mathbf{r}', t')}{\partial t'} \right|_{t' = t - (|\mathbf{r} - \mathbf{r}'|/c)}. \qquad (5)$$

The heating function can be written as the product of a spatial absorption function and a temporal illumination function

$$H(\mathbf{r}, t) = A(\mathbf{r})I(t). \qquad (6)$$

Thus, $p(\mathbf{r}, t)$ can be expressed as

$$p(\mathbf{r}, t) = \frac{\beta}{4\pi C_p} \iiint \frac{d^3 r'}{|\mathbf{r} - \mathbf{r}'|} A(\mathbf{r}')I'(t') \qquad (7)$$

where $I'(t') = dI(t')/dt'$.

B. Exact Reconstruction Theory

We first solve the problem where the pulse pumping is a Dirac delta function

$$I(t) = \delta(t). \qquad (8)$$

Suppose the detection point on the spherical surface $\mathbf{r} = \mathbf{r}_0$, which encloses the sample (Fig. 1). By dropping the primes, (7) may be rewritten as

$$p(\mathbf{r}_0, t) = \eta \iiint d^3 r A(\mathbf{r}) \frac{\delta'\left(t - \frac{|\mathbf{r}_0 - \mathbf{r}|}{c}\right)}{4\pi|\mathbf{r}_0 - \mathbf{r}|} \qquad (9)$$

where $\eta = \beta/C_p$. The inverse problem is to reconstruct the absorption distribution $A(\mathbf{r})$ from a set of data $p(\mathbf{r}_0, t)$ measured at positions $\mathbf{r}_0$. Taking the Fourier transform on variable t of (9), and denoting $k = \omega/c$, we get

$$\tilde{p}(\mathbf{r}_0, \omega) = -i\omega\eta \iiint d^3 r A(\mathbf{r}) \frac{\exp(ik|\mathbf{r}_0 - \mathbf{r}|)}{4\pi|\mathbf{r}_0 - \mathbf{r}|} \qquad (10)$$
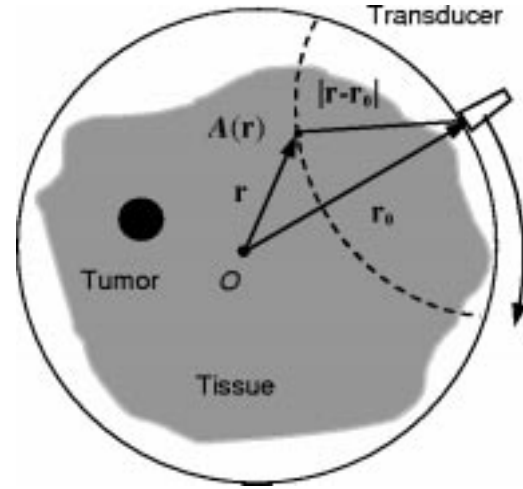

Fig. 1. Acoustic detection scheme. The ultrasonic transducer at position $\mathbf{r}_0$ records the thermoacoustic signals on a spherical surface with radius $|\mathbf{r} - \mathbf{r}_0|$.

where the following Fourier transform pair exists:

$$\tilde{p}(\mathbf{r}_0, \omega) = \int_{-\infty}^{+\infty} p(\mathbf{r}_0, t) \exp(i\omega t) \, dt, \qquad (11a)$$

$$p(\mathbf{r}_0, t) = \frac{1}{2\pi} \int_{-\infty}^{+\infty} \tilde{p}(\mathbf{r}_0, \omega) \exp(-i\omega t) \, d\omega. \qquad (11b)$$

We next derive the exact solution using the spherical harmonic function basis. In the derivation, we referred to the mathematical techniques for ultrasonic reflectivity imaging [11]. The mathematics utilized can also be found routinely in the mathematical literature, such as [12]. Here, we list the identities (12a)–(12f) used in the subsequent deduction:

1) The complete orthogonal integral of spherical harmonics $Y_l^m(\theta_0, \varphi_0)$

$$\iint_{\Omega_0} Y_l^m(\theta_0, \varphi_0) Y_k^{n^*}(\theta_0, \varphi_0) \, d\Omega_0 = \delta_{l,k}\delta_{m,n} \qquad (12a)$$

where $d\Omega_0 = \sin\theta_0 \, d\theta_0 \, d\varphi_0$ and $*$ denotes the complex conjugate.

2) The Legendre polynomial

$$P_l(\mathbf{n} \cdot \mathbf{n}_0) = \frac{4\pi}{2l+1} \sum_{m=-l}^{+l} Y_l^m(\theta, \varphi) Y_l^{m^*}(\theta_0, \varphi_0) \qquad (12b)$$

where the unit vectors $\mathbf{n}$ and $\mathbf{n}_0$ point in the directions (θ, φ) and (θ_0, φ_0), respectively.

3) The orthogonal integral of Legendre polynomials, derived from (12a) and (12b)

$$\iint_{\Omega_0} d\Omega_0 P_l(\mathbf{n} \cdot \mathbf{n}_0) P_m(\mathbf{n}' \cdot \mathbf{n}_0) = \frac{4\pi}{2l+1} \delta_{lm} P_l(\mathbf{n} \cdot \mathbf{n}') \qquad (12c)$$

where the unit vector $\mathbf{n}' = \mathbf{r}'/r'$ points in the direction (θ', φ').

4) The expansion identity

$$\frac{\exp(ik|\mathbf{r}_0 - \mathbf{r}|)}{4\pi|\mathbf{r}_0 - \mathbf{r}|} = \frac{ik}{4\pi} \sum_{l=0}^{\infty} (2l+1) j_l(kr) h_l^{(1)}(kr_0) P_l(\mathbf{n} \cdot \mathbf{n}_0),$$
$$(k > 0) \qquad (12d)$$

where $\mathbf{n} = \mathbf{r}/r$, $\mathbf{n}_0 = \mathbf{r}_0/r_0$, $j_l(\cdot)$ and $h_l^{(1)}(\cdot)$ are the spherical Bessel and Hankel functions, respectively.

5) The complete orthogonal integral of Bessel functions

$$\int_0^{+\infty} dk k^2 j_m(kr) j_m(kr') = \frac{\pi}{2r^2} \delta(r - r'). \quad (12e)$$

6) The summation identity of Legendre polynomials

$$\sum_{m=0}^{\infty} (2m+1) P_m(\mathbf{n} \cdot \mathbf{n}') = \frac{4\pi \delta(\theta - \theta') \delta(\varphi - \varphi')}{\sin \theta}. \quad (12f)$$

First, substituting (12d) into (10), we obtain

$$\tilde{p}(\mathbf{r}_0, \omega) = \frac{\omega k \eta}{4\pi} \iiint d^3 r A(\mathbf{r}) \sum_{l=0}^{\infty} (2l+1) j_l(kr) \\ \cdot h_l^{(1)}(kr_0) P_l(\mathbf{n} \cdot \mathbf{n}_0). \quad (13)$$

Then, multiplying both sides of (13) by $P_m(\mathbf{n}' \cdot \mathbf{n}_0)$, and integrating with respect to $\mathbf{n}_0$ over the surface of the sphere, and considering the identity (12c), we obtain

$$\iint_{\Omega_0} d\Omega_0 \tilde{p}(\mathbf{r}_0, \omega) P_m(\mathbf{n}' \cdot \mathbf{n}_0)$$

$$= \frac{\omega k \eta}{4\pi} \iiint d^3 r A(\mathbf{r}) \sum_{l=0}^{\infty} (2l+1) j_l(kr) h_l^{(1)}(kr_0)$$

$$\cdot \iint_{\Omega_0} d\Omega_0 P_l(\mathbf{n} \cdot \mathbf{n}_0) P_m(\mathbf{n}' \cdot \mathbf{n}_0)$$

$$= \frac{\omega k \eta}{4\pi} \iiint d^3 r A(\mathbf{r}) \sum_{l=0}^{\infty} (2l+1) j_l(kr) h_l^{(1)}(kr_0) \frac{4\pi}{2l+1}$$

$$\cdot \delta_{lm} P_l(\mathbf{n} \cdot \mathbf{n}')$$

$$= k^2 \eta c \iiint d^3 r A(\mathbf{r}) j_m(kr) h_m^{(1)}(kr_0) P_m(\mathbf{n} \cdot \mathbf{n}')$$

i.e.,

$$\iint_{\Omega_0} d\Omega_0 \tilde{p}(\mathbf{r}_0, \omega) P_m(\mathbf{n}' \cdot \mathbf{n}_0) \frac{1}{h_m^{(1)}(kr_0)}$$

$$= k^2 \eta c \iiint d^3 r A(\mathbf{r}) j_m(kr) P_m(\mathbf{n} \cdot \mathbf{n}'). \quad (14)$$

Further, multiplying both sides of (14) by $j_m(kr')$, integrating them with respect to k from zero to $+\infty$, and then multiplying both sides of (14) again by $(2m+1)$ and summing m from zero to ∞, and considering the identity (12e) and (12f), we get

$$\iint_{\Omega_0} d\Omega_0 \int_0^{+\infty} dk \tilde{p}(\mathbf{r}_0, \omega) \sum_{m=0}^{\infty} \frac{(2m+1) j_m(kr')}{h_m^{(1)}(kr_0)} P_m(\mathbf{n}' \cdot \mathbf{n}_0)$$

$$= \eta c \iiint d^3 r A(\mathbf{r}) \sum_{m=0}^{\infty} (2m+1) P_m(\mathbf{n} \cdot \mathbf{n}') \int_0^{+\infty} dk k^2 \\ \cdot j_m(kr') j_m(kr)$$

$$= \eta c \iiint d^3 r A(\mathbf{r}) \frac{4\pi \delta(\theta - \theta') \delta(\varphi - \varphi')}{\sin \theta} \frac{\pi}{2r^2} \delta(r - r')$$

$$= 2\pi^2 \eta c A(\mathbf{r}').$$

Finally, dropping the primes, we can rewrite the equation as

$$A(\mathbf{r}) = \frac{1}{2\pi^2 \eta c} \iint_{\Omega_0} d\Omega_0 \int_0^{+\infty} dk \tilde{p}(\mathbf{r}_0, \omega) \\ \cdot \sum_{m=0}^{\infty} \frac{(2m+1) j_m(kr)}{h_m^{(1)}(kr_0)} P_m(\mathbf{n} \cdot \mathbf{n}_0). \quad (15)$$

This is the exact inverse solution of (9). It involves summation of a series and may take much time to compute. Therefore, it is desirable to further simplify the solution.

C. Modified Backprojection

In experiments, the detection radius r_0 is usually much larger than the wavelengths of the thermoacoustic waves that are useful for imaging. Because the low-frequency component of the thermoacoustic signal does not significantly contribute to the spatial resolution, it can be removed by a filter. Therefore, we can assume $|k| r_0 \gg 1$ and use the asymptotic form of the Hankel function to simplify (15). The following two identities are involved [12]:

1) The expansion identity similar to (12d)

$$\frac{\exp(-ik|\mathbf{r}_0 - \mathbf{r}|)}{4\pi |\mathbf{r}_0 - \mathbf{r}|} = \frac{-ik}{4\pi} \sum_{m=0}^{\infty} (2m+1) j_m(kr) \\ \cdot h_m^{(2)}(kr_0) P_m(\mathbf{n} \cdot \mathbf{n}_0), \quad (k > 0). \quad (16a)$$

2) The approximation when $|k| r_0 \gg 1$

$$h_m^{(1)}(kr_0) \approx \frac{1}{h_m^{(2)}(kr_0)} \left(\frac{1}{(kr_0)^2} + O\left(\frac{1}{(kr_0)^4} \right) \right) \quad (16b)$$

where $h_l^{(2)}(\cdot)$ is the spherical Hankel function of the second kind.

Substituting (16b) into (15), we get

$$A(\mathbf{r}) \approx \frac{1}{2\pi^2 \eta c} \iint_{\Omega_0} d\Omega_0 \int_0^{+\infty} dk \tilde{p}(\mathbf{r}_0, \omega) k^2 r_0^2 \sum_{m=0}^{\infty} (2m+1) \\ \cdot j_m(kr) h_m^{(2)}(kr_0) P_m(\mathbf{n} \cdot \mathbf{n}_0). \quad (17)$$

Considering the form of (16a), the above equation can be rewritten as

$$A(\mathbf{r}) = \frac{r_0^2}{2\pi^2 \eta c} \iint_{\Omega_0} d\Omega_0 \int_0^{+\infty} dk \tilde{p}(\mathbf{r}_0, \omega)(ik)$$

$$\cdot \frac{\exp(-ik|\mathbf{r}_0 - \mathbf{r}|)}{|\mathbf{r}_0 - \mathbf{r}|}$$

$$= -\frac{r_0^2}{\pi \eta c^3} \iint_{\Omega_0} d\Omega_0 \frac{1}{2\pi} \int_0^{+\infty} d\omega \tilde{p}(\mathbf{r}_0, \omega)(-i\omega)$$

$$\cdot \frac{\exp\left(-i\omega \frac{|\mathbf{r}_0 - \mathbf{r}|}{c}\right)}{|\mathbf{r}_0 - \mathbf{r}|}.$$

Because $p(\mathbf{r}, t)$ is a real function, $p^*(\mathbf{r}, \omega) = p(\mathbf{r}, -\omega)$. Taking the summation of the above equation with its complex conjugate and then dividing it by two, we get

$$A(\mathbf{r}) = \frac{r_0^2}{4\pi^2 \eta c} \iint_{\Omega_0} d\Omega_0 \int_{-\infty}^{+\infty} dk \tilde{p}(\mathbf{r}_0, \omega)(ik)$$

$$\cdot \frac{\exp(-ik|\mathbf{r}_0 - \mathbf{r}|)}{|\mathbf{r}_0 - \mathbf{r}|}$$

$$= -\frac{r_0^2}{2\pi \eta c^3} \iint_{\Omega_0} d\Omega_0 \frac{1}{2\pi} \int_{-\infty}^{+\infty} d\omega \tilde{p}(\mathbf{r}_0, \omega)(-i\omega)$$

$$\cdot \frac{\exp\left(-i\omega \frac{|\mathbf{r}_0 - \mathbf{r}|}{c}\right)}{|\mathbf{r}_0 - \mathbf{r}|}.$$

Recalling the inverse Fourier transform (11b), we get

$$A(\mathbf{r}) = -\frac{r_0^2}{2\pi\eta c^3} \iint\limits_{\Omega_0} d\Omega_0 \frac{1}{|\mathbf{r}_0 - \mathbf{r}|} \frac{\partial p(\mathbf{r}_0, t)}{\partial t}\bigg|_{t=|\mathbf{r}_0-\mathbf{r}|/c} \quad (18)$$

i.e.,

$$A(\mathbf{r}) = -\frac{r_0^2}{2\pi\eta c^4} \iint\limits_{\Omega_0} d\Omega_0 \frac{1}{t} \frac{\partial p(\mathbf{r}_0, t)}{\partial t}\bigg|_{t=|\mathbf{r}_0-\mathbf{r}|/c}. \quad (19)$$

Equation (19) shows that the absorption distribution can be calculated in the time domain by the means of backprojection and coherent summation over spherical surfaces of the quantity $-(1/t)(\partial p(\mathbf{r}_0, t)/\partial t)$ instead of the acoustic pressure itself. This approximate algorithm requires less computing time than the exact solution (15).

For initial investigations, we measure the samples in a circular configuration. In these cases, the backprojection is carried out in a circle around the slices, and (19) can be simplified to

$$A(\mathbf{r}) = -\frac{r_0^2}{2\pi\eta c^4} \int_{\varphi_0} d\varphi_0 \frac{1}{t} \frac{\partial p(\mathbf{r}_0, t)}{\partial t}\bigg|_{t=|\mathbf{r}_0-\mathbf{r}|/c}. \quad (20)$$

III. EXPERIMENTAL METHOD

A. Diagram of Setup

Fig. 2 shows the experimental setup for the circular measurement configuration, which is modified from our previous paper [7]. For the convenience of the reader, the system is briefly described here. The unfocused transducer (V323, Panametrics) has a central frequency of 2.25 MHz and a diameter of 6 mm. It is fixed and it points horizontally to the center of the rotation stage, which is used to hold the samples. For good coupling of acoustic waves, both the transducer and the sample are immersed in mineral oil in a container.

The microwave pulses are transmitted from a 3-GHz microwave generator with a pulse energy of 10 mJ and a width of 0.5 μs, and then delivered to the sample from the bottom by a rectangular waveguide with a cross section of 72 mm × 34 mm. A function generator (Protek, B-180) is used to trigger the microwave generator, control its pulse repetition frequency, and synchronize the oscilloscope sampling. The signal from the transducer is first amplified through a pulse amplifier, then recorded and averaged 200 times by an oscilloscope (TDS640A, Tektronix). A personal conputer is used to control the step motor for rotating the sample and transferring the data.

Last, we want to point out that, in our experiments, the smallest distance r_0 between the rotation center and the surface of the transducer is 4.3 cm. In the frequency domain (100 KHz– 1.8 MHz), $|k|r_0 = 2\pi r_0 f/c$ with 1.5 mm/μs, we get $18 < |k|r_0 < 330$. Therefore, the required condition $|k|r_0 \gg 1$ for the modified backprojection algorithm is satisfied.

B. Technical Consideration

During measurement, we find that the piezoelectric signal $S_0(\mathbf{r}_0, t)$ detected by the transducer includes the thermal acoustic signal $S(\mathbf{r}_0, t)$ as well as some noise. The noise comes from two contributors. One is the background random noise of the measurement system, which can be suppressed by averaging the measured data. The other part, $S_{mp}(t)$, results from the microwave pumping via electromagnetic induction.
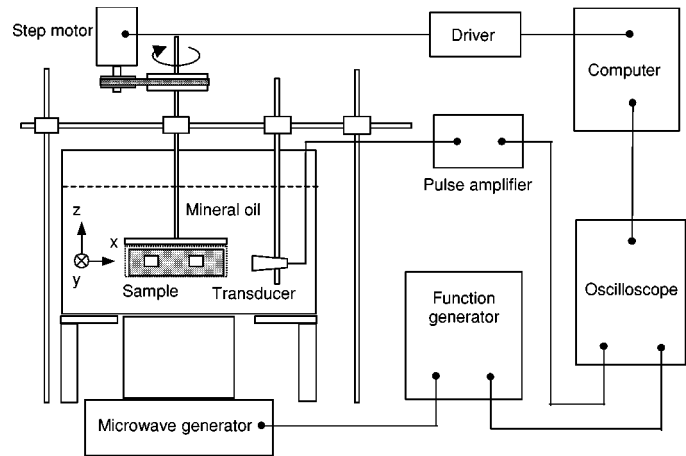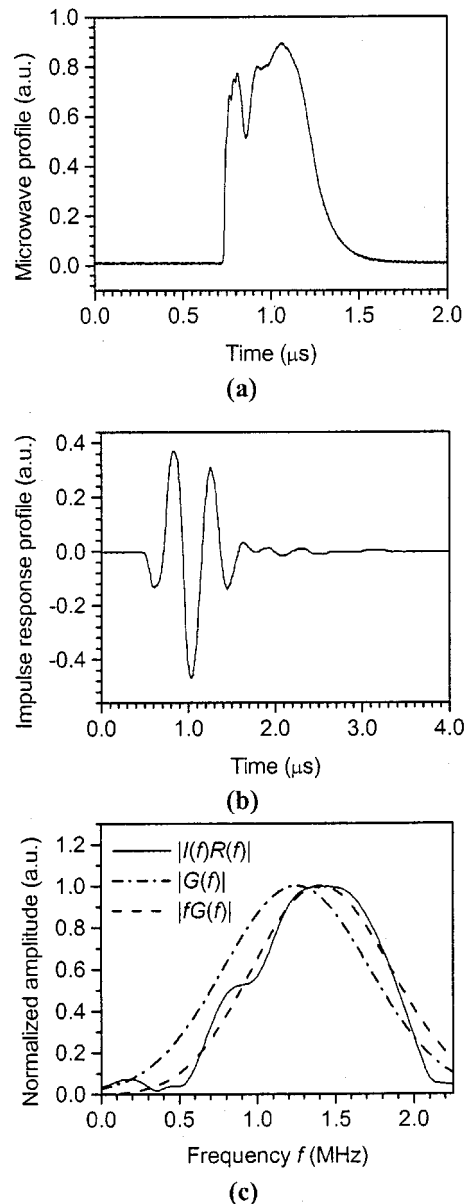

Fig. 2. The experimental setup.

Fig. 3. (a) The temporal profile of the microwave pulse; (b) the temporal profile of the impulse response of the transducer; (c) compare the normalized amplitudes of the spectrum $I(f)R(f)$, $G(f)$ and $fG(f)$.

The pumping component of the noise can be measured without a sample, and can be subtracted from the measured data

$$S(\mathbf{r}_0, t) \approx S_0(\mathbf{r}_0, t) - S_{mp}(t). \tag{21}$$

In fact, the transducer is not a real point detector. For simplicity, we can ignore its size if we put it far away from the sample. However, we still have to consider the impulse response $R(t)$ of the transducer and the pumping duration $I(t)$ of the microwave pulse. In general, the measured thermoacoustic signal can be written as a convolution

$$S(\mathbf{r}_0, t) = p(\mathbf{r}_0, t) * I(t) * R(t) \tag{22}$$

where $p(\mathbf{r}_0, t)$ is the thermoacoustic signal with delta-pulse microwave pumping. In the frequency domain, (22) can be written as

$$S(\mathbf{r}_0, \omega) = p(\mathbf{r}_0, \omega)I(\omega)R(\omega) \tag{23}$$

where

$$I(\omega) = \int_{-\infty}^{+\infty} I(t) \exp(i\omega t)\, dt, \tag{24a}$$

$$R(\omega) = \int_{-\infty}^{+\infty} R(t) \exp(i\omega t)\, dt. \tag{24b}$$

Because of the presence of noise and the finite bandwidth of $I(\omega)$ and $R(\omega)$, an appropriate deconvolution algorithm should be used to calculate $p(\mathbf{r}_0, \omega)$. In the reconstruction, only the high-frequency component of the thermoacoustic signal is required. Therefore, we compute $p(\mathbf{r}_0, \omega)G(\omega)$ instead, where $G(\omega)$ is a high-frequency bandpass filter such as a Gaussian filter

$$G(\omega) = \exp\left[-\alpha\left(\frac{\omega}{\omega_0} - 1\right)^2\right]$$

and α and ω_0 are two parameters of the filter, $\omega = 2\pi f$ and $\omega_0 = 2\pi f_0$.

In our experiments, $I(t)$ is approximately a rectangular function with duration $\tau = 0.5\ \mu s$ and its temporal profile is shown in Fig. 3(a). Its spectrum $I(\omega)$ covers the range from 0 to 2 MHz. The transducer that we used is of the videoscan type with a central frequency of $f_0 = 2.25$ MHz, and the temporal profile of the impulse response is shown in Fig. 3(b). It is observed that the generated thermoacoustic signal under microwave pumping with duration $\tau = 0.5\ \mu s$ exists primarily in a frequency range below 1.8 MHz. We chose the parameters $\alpha = 3.6$ and $f_0 = 1.25$ MHz in the Gaussian filter

$$G(f) = \exp\left[-\alpha\left(\frac{f}{f_0} - 1\right)^2\right]$$

to eliminate the noise at high as well as low frequencies. The spectrum $G(f)$ is shown as the dash-dot line in Fig. 3(c). We compared the normalized spectrum $I(f)R(f)$ [solid line in Fig. 3(c)] with $fG(f)$ [dash line in Fig. 3(c)], and found $|fG(f)| \approx |I(f)R(f)|$ when $f < 2$ MHz. Of course, this approximated equality is a special case for our measurement system only. Therefore, the filtered $\partial p(\mathbf{r}_0, t)/\partial t$ can be simply calculated by an inverse fast Fourier transform (IFFT)

$$\frac{\partial p(\mathbf{r}_0, t)}{\partial t} \approx \text{IFFT}\left\{S(\mathbf{r}_0, \omega)F(\omega)\right\} \tag{25}$$
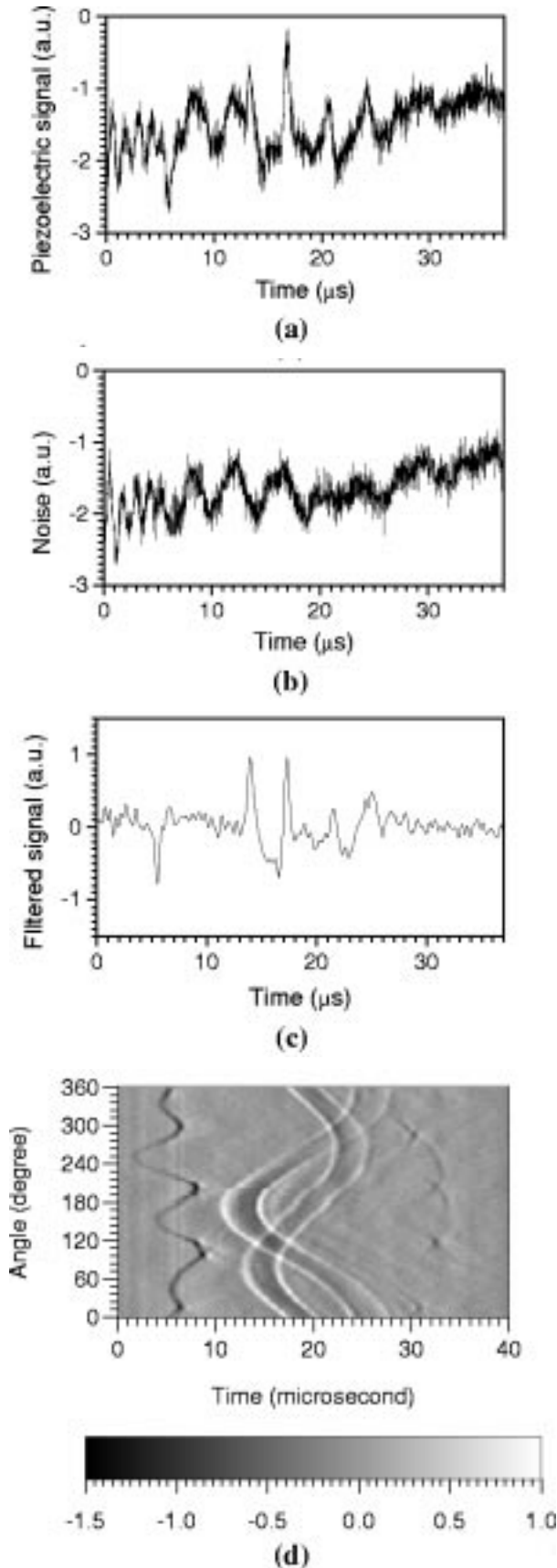

Fig. 4. (a) An example of temporal piezoelectric signal; (b) an example of temporal noise; (c) an example of filtered signal; and (d) an example of filtered thermoacoustic signals detected at different angular positions from 0° to 360°.
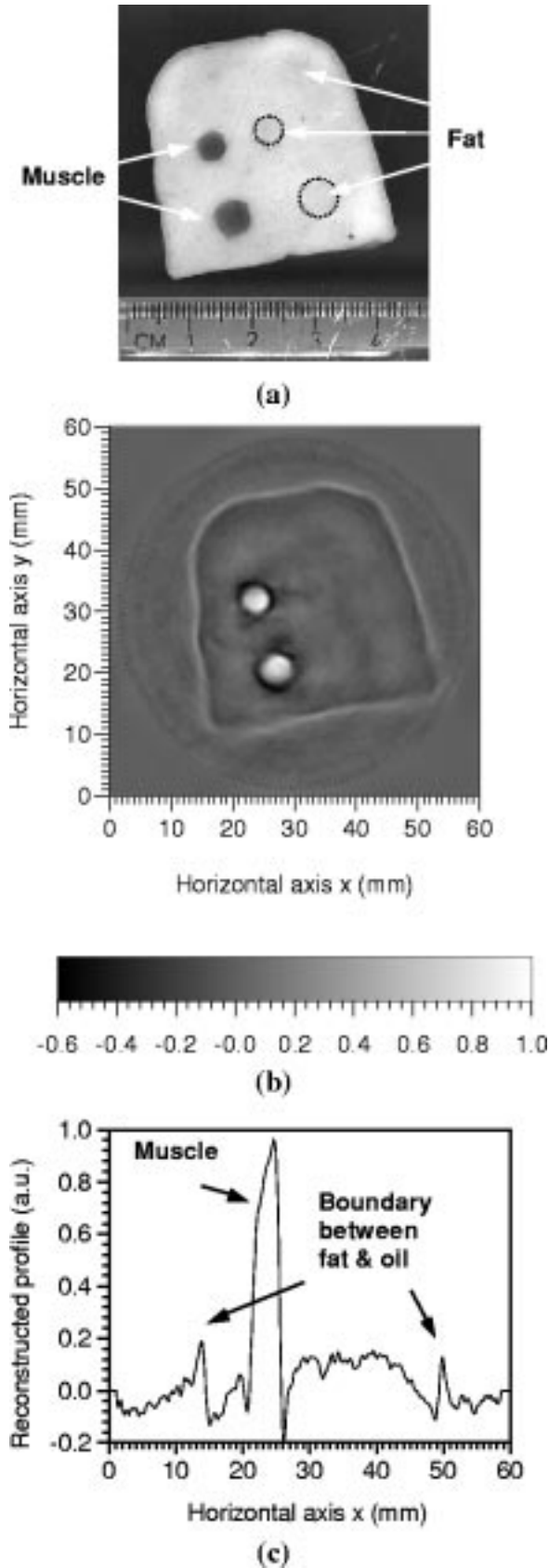
Muscle

Fat

(a)

(b)

(c)

Fig. 5. (a) Cross section of a tissue sample; (b) reconstructed image; and (c) a line profile of the reconstructed image at $y = 31.5$ mm.

where $F(\omega)$ is a wide bandpass filter, which is used to further eliminate noise at high and low frequencies in order to guarantee

the condition $|k|r_0 \gg 1$ for the modified backprojection. A simple filter is

$$F(f) = \begin{cases} 1, & 0.1 \text{ MHz} < f < 1.8 \text{ MHz} \\ 0, & \text{otherwise.} \end{cases} \tag{26}$$

IV. RESULTS AND DISCUSSION

Finally, we use the above modified backprojection algorithm and the experimental method to investigate some tissue samples.

A. Experimental Data Preprocessing

The measured piezoelectric data include the useful thermoacoustic signal as well as some noise data as illustrated by the following example. Fig. 4(a) is a typical measured temporal piezoelectric signal, which is from the sample shown in Fig. 5(a). One portion of the noise resulting from the microwave pumping looks like the curve in Fig. 4(b), which is acquired at the same sampling rate and the same delay time with the transducer in the same position as the curve in Fig. 4(a). Because the slice is very thin, the thermoacoustic signal is not much higher than the noise resulting from the microwave pumping. Next, we subtract the noise from the raw thermoacoustic signal and use a wide bandpass filter to eliminate some of the useless low-frequency and high-frequency components. This processed data is shown in Fig. 4(c); it is much cleaner than the raw data in Fig. 4(a). The filtered thermoacoustic signals detected at different angular positions from 0° to 360° are shown in Fig. 4(d).

B. Image Contrast

Image contrast is an important index for biological imaging. Fig. 5(a) shows a tested sample, which was photographed after the experiment. The sample was made according to the following procedure. First, we cut a thin piece of homogeneous pork fat tissue and shaped it arbitrarily to form a base. Its thickness is 5 mm and its maximum diameter is 4 cm. Then we used different screwdrivers to carefully make two pairs of holes that were approximately 4 and 6 mm in diameter, respectively. Finally, one big and one small hole on the left side were filled with pork muscle, while the two holes on the right side were filled with pork fat of the same type as that which made up the base.

In the experiment, the transducer rotationally scanned the sample from 0° to 360° with a step size of 2.25°. The detection radius r_0 was 4.3 mm. We used the 160 series of data as shown in Fig. 4(d) to calculate the image by our modified backprojection method.

The reconstructed image is shown in Fig. 5(b). The outline and size of the fat base as well as the sizes and locations of the two muscle pieces are in good agreement with the original sample in Fig. 5(a). Fig. 5(c) shows a line profile for the small piece of muscle in the image. It indicates that the contrast between the fat and the muscle is very high. This high contrast is due to the low microwave absorption capacity of fat and the high absorption capacity of muscle: at 3 GHz, the penetration depth for muscle and fat are 1.2 and 9 cm, respectively. However, the two pieces of fat are not visible in the image [Fig. 5(b)], which means the minute mechanical discontinuity between the boundaries of muscle and fat does not contribute much to the

thermoacoustic signal. On the contrary, discontinuity improves the strength of the echo sounds in pure ultrasound imaging.

C. Spatial Resolution

Spatial resolution is another important index for biological imaging. We used samples with a set of small thermoacoustic sources to test the resolution. One tested sample is shown in Fig. 6(a), which was also photographed after the experiment was completed.

The sample was made according to the following procedure. First, we cut a thin piece of homogeneous pork fat tissue and made it into an arbitrary shape. Its thickness was 5 mm with a maximum diameter of 4 cm. Then we used a small screwdriver to carefully make a set of small holes about 2 mm in diameter. In the meantime, we prepared a hot solution with 5% gelatin, 0.8% salt, and a drop of dark ink (to improve the photographic properties of the sample). Next, we used an injector to inject a drop of the gelatin solution into each small hole and subsequently blew out the air to make good coupling between the gelatin solution and the fat tissue. After being cooled in room temperature for about 15 min, the gelatin solution was solidified. During the experiment, the transducer also rotationally scanned the sample from $0°$ to $360°$ with a step size of $2.25°$. The detection radius r_0 was 4.3 mm.

The reconstructed image produced by our modified backprojection method is shown in Fig. 6(b); it also agrees with the original sample well. In particular, the relative locations and sizes of those small thermoacoustic sources are clearly resolved and perfectly match the original ones. Fig. 6(c) shows a reconstructed profile (solid curve) at position $x = 27.45$ mm of the image Fig. 6(b), which includes two gelatin sources with a distance of about 3 mm. Each gelatin source has a distinct profile in the image. The boundaries between them are clearly imaged. Moreover, the reconstructed profile is in good agreement with the original profile (dashed curve), which was a grayscale profile of the image Fig. 6(b). The half-amplitude line cuts across the reconstructed profile at points B_1, A_1, A_2, and B_2, respectively. The distances $|A_1B_1| = 1.72$ mm and $|A_2B_2| = 1.67$ mm in the image are close to the original values of about 1.80 and 1.60 mm, respectively, which were measured in the original objects. Therefore, the width of the profile at the half-amplitude closely measures its physical size.

We here define a resolving criterion to estimate the spatial resolution. The quarter-amplitude line cuts across the profiles at points C_1 and C_2, respectively, as shown in Fig. 6(c). If the right source moves to the position of the left one, the reconstructed profile is equal to the spatial summation of the profiles of the two sources, because of the linear superposition property of acoustic waves. When point C_2 encounters C_1, the new amplitude at C_2 or C_1 would reach the half amplitude, and the two sources could still be differentiated. If the right one moves more to the left, the new amplitude between their overlap regions would elevate to more than the half amplitude. When we use a half-amplitude line to cut across the profiles, we get only two points on the far side of each profile, which means that these two sources can no longer be clearly distinguished. Further, when point A_1 touches A_2, these two sources join as a single object in the image.
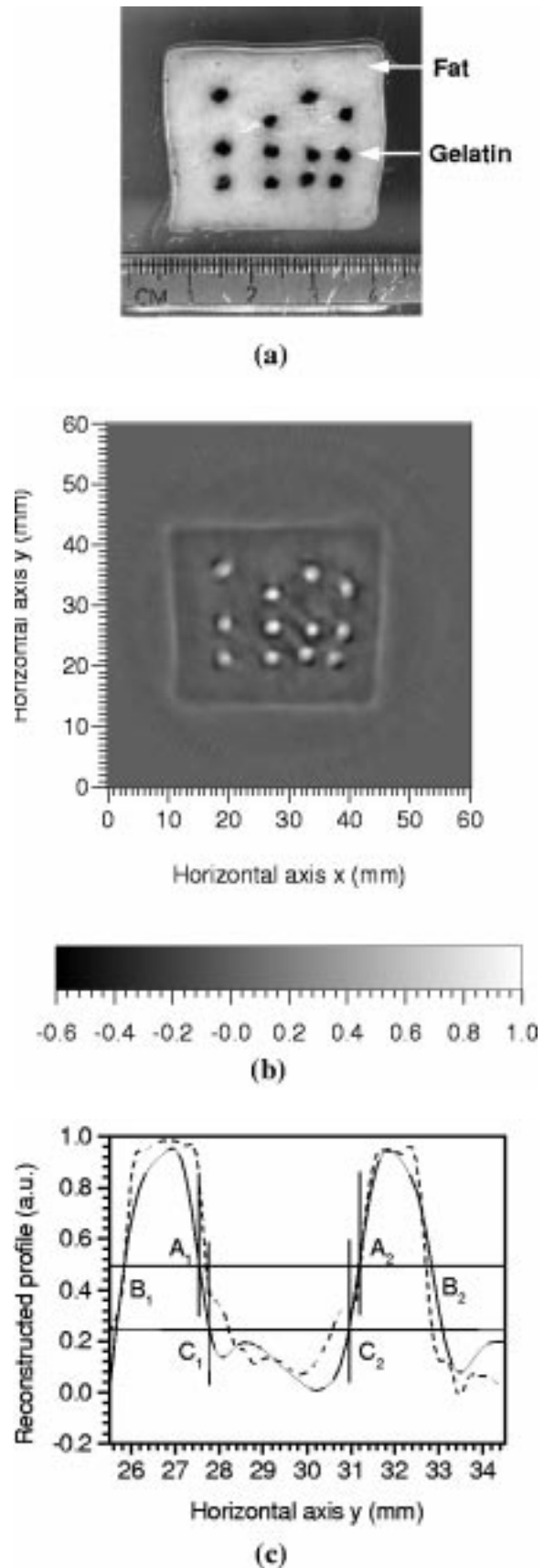

Fig. 6.   (a) Cross section of a tissue sample; (b) reconstructed image; and (c) comparison between a line profile (solid curve) of the reconstructed image (b) at $x = 27.45$ mm and the corresponding grayscale profile (dashed curve) of the original image (a).
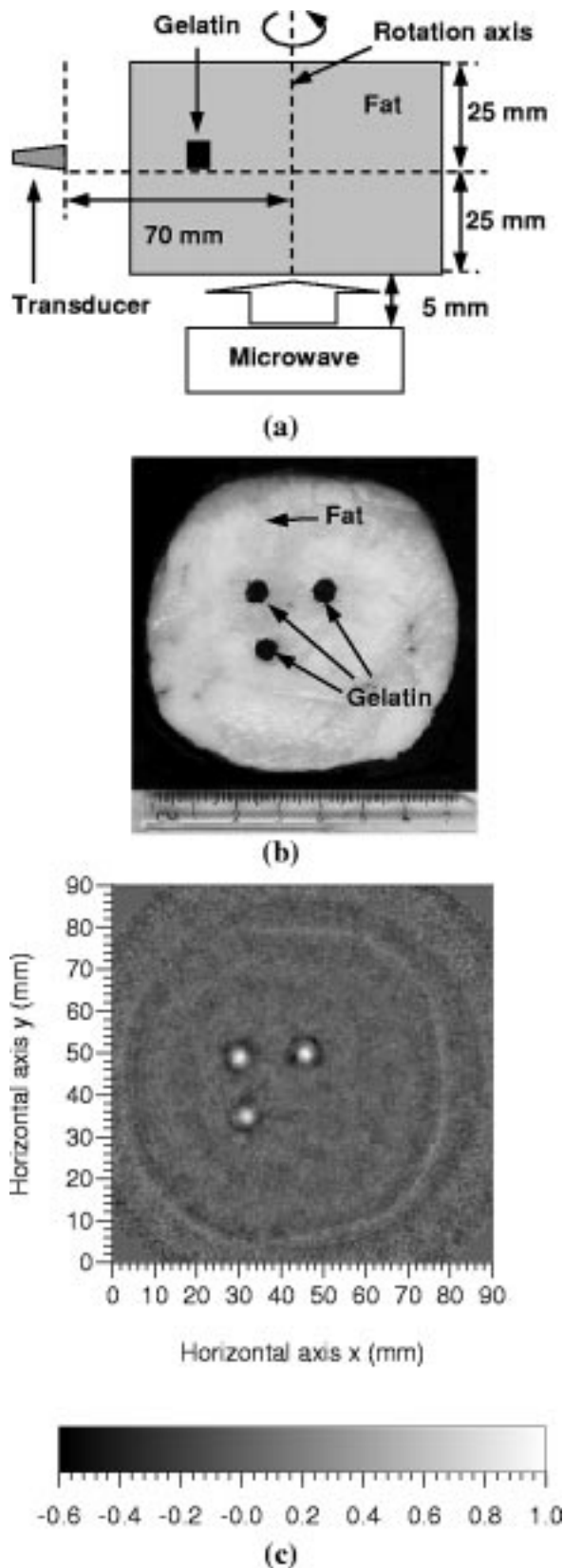
Fig. 7. (a) Diagram of the sample structure and the measurement; (b) cross section of the tissue sample; and (c) reconstructed image.

Therefore, the minimum distance that can be differentiated is approximately equal to the summation of the horizontal distance between point A_1 and C_1 and the horizontal distance between

point A_2 and C_2. We have checked additional pairs of sources resembling those in the image of Fig. 6(b), and found that this minimum distance is less than 0.5 mm. We can, therefore, claim that the spatial resolution in our system reaches less than 0.5 mm, which agrees with the theoretical spatial resolution limit for 1.8-MHz signals whose half wavelength is $\sim$0.5 mm with the sound speed of 1.5 mm/μs.

Of course, the detecting transducer has a finite physical size. If it is close to the thermoacoustic sources, it cannot be approximated as a point detector. Its size will blur the images and decrease the spatial resolution. Therefore, in experiments, the transducer must be placed some distance away from the tissue samples. In general, due to the finite size of the transducer, the farther away the transducer is from the detection center, the better the resolution at the expense of the signal strength.

Other limiting factors of spatial resolution include the duration of the microwave pulse and the impulse response of the transducer. In general, using a shorter microwave pulse will produce more high-frequency components in the thermoacoustic signals. The disadvantages resulting from employing a shorter pulse, however, are insufficient energy delivery and a decrease in the signal-to-noise ratio. Selection of the duration of the pulse is dependent on the experimental conditions and measurement systems. In biological tissues, microwaves at 300 MHz$\sim$3 GHz with 0.1$\sim$1 μs pulse width are often adopted. Therefore, the high-frequency of the thermoacoustic signals reaches several MHz. Such a wide-band transducer for measuring acoustic waves at $\sim$MHz is widely available.

D. Thick Sample

The advantage of using microwave is its long penetration depth in soft tissue. A microwave can reach a tumor buried inside tissue and heat it to generate thermoacoustic waves. One tested sample is shown in Fig. 7(a). The experiment was conducted according to a procedure similar to the one above. Three small absorbers were buried inside a big fat base. The big pork fat tissue had a maximum diameter of 7 cm. Screwdrivers were used to carefully make three holes about 5 mm in diameter with a depth of 2.5 cm. Next, an injector was used to inject a drop of the same gelatin solution as above into each small hole, and, subsequently, air was blown out to improve the coupling between the gelatin solution and the fat tissue. These gelatin sources were about 5 mm in diameter. After being cooled at room temperature for about 15 min, the gelatin solutions solidified. The photograph of the sample at this stage is shown in Fig. 7(b). Finally, the holes were filled with fat, and the gelatin sources were buried in the fat tissue.

During the experiment, a microwave was transmitted out to the sample from below. The transducer rotationally scanned the sample, including the gelatin sources, from 0° to 360° in a plane as Fig. 7(a) shows. The distance between the transducer and the rotation center was 7 cm. The reconstructed image produced by our modified backprojection method, which agrees well with the original sample, is shown in Fig. 7(c).

The above experiments verified the principle of the modified backprojection algorithm, which implies back projection and coherent summation over spherical surfaces. In particular, a set of circular measurement data would be sufficient to yield a

satisfactory cross-sectional image for a sample with only small absorption sources in the same horizontal plane and a lower absorption background. Of course, for a complicated sample, data from only a circular measurement would be insufficient for 3-D reconstruction unless cylindrical focusing is employed. This limited view problem will be addressed in our future work.

Finally, we must point out that an inhomogeneous acoustic property, such as the speed of sound variation, might result in reconstruction errors. Fortunately, the speed of sound in most soft tissue is relatively constant at ~ 1.5 mm/μs. The above experiments demonstrated that the small speed variations between fat and muscle or gelatin did not result in significant reconstruction artifacts. The reason is that thermoacoustic waves are produced internally by microwave absorption and are propagated one-way to the detectors. Thus, a small speed variation does not affect the travel time of the sound very much in a finite-length path, for example, 10 cm, which is comparable to a typical breast diameter. Therefore, in thermoacoustic tomography, satisfactory contrast and resolution are obtainable even in tissue with a small degree of acoustic inhomogeneity.

V. CONCLUSION

Pulsed-microwave-induced thermoacoustic tomography of inhomogeneous tissues has been studied. Both an exact inverse solution and a modified backprojection algorithm have been derived, which are based on the data acquired by wide-band point detectors on a spherical surface that encloses the sample under study. A set of experiments on tissue samples has been investigated under a circular measurement configuration. The reconstructed images calculated by the modified backprojection method agree well with the original ones. Results indicate that this technique using reconstruction theory is a powerful imaging method that results in good contrast and good spatial resolution (0.5 mm), which can be used for the investigation of tissues with inhomogeneous microwave absorptions.

REFERENCES

[1] L. E. Larsen and J. H. Jacobi, *Medical Applications of Microwave Imaging*. Piscataway, NJ: IEEE Press, 1986.

[2] K. D. Paulsen and P. M. Meaney, "Nonactive antenna compensation for fixed-array microwave imaging Part I: Model development," *IEEE Trans. Med. Imag.*, vol. 18, pp. 496–507, June 1999.

[3] P. M. Meaney, K. D. Paulsen, J. T. Chang, M. W. Fanning, and A. Hartov, "Nonactive antenna compensation for fixed-array microwave imaging: Part II Imaging results," *IEEE Trans. Med. Imag.*, vol. 18, pp. 508–518, June 1999.

[4] F. W. Kremkau, *Diagnostic Ultrasound: Principles and Instruments*. Philadelphia, PA: W. B. Saunders, 1993.

[5] E. Steen and B. Olstad, "Volume rendering of 3D medical ultrasound data using direct feature mapping," *IEEE Trans. Med. Imag.*, vol. 13, pp. 517–525, June 1994.

[6] G. Ku and L. V. Wang, "Scanning microwave-induced thermoacoustic tomography: Signal, resolution, and contrast," *Med. Phys.*, vol. 28, pp. 4–10, 2001.

[7] M. H. Xu, G. Ku, and L. V. Wang, "Microwave-induced thermoacoustic tomography using multi-sector scanning," *Med. Phys.*, vol. 28, pp. 1958–1963, 2001.

[8] C. G. A. Hoelen and F. F. M. de Mul, "Image reconstruction for photoacoustic scanning of tissue structures," *Appl. Opt.*, vol. 39, no. 31, pp. 5872–5883, Nov. 2000.

[9] Y. V. Zhulina, "Optimal statistical approach to optoacoustic image reconstruction," *Appl. Opt.*, vol. 39, no. 32, pp. 5971–5977, Nov. 2000.

[10] R. A. Kruger, D. R. Reinecke, and G. A. Kruger, "Thermoacoustic computed tomography-technical considerations," *Med. Phys.*, vol. 26, no. 9, pp. 1832–1837, 1999.

[11] S. J. Norton and M. Linzer, "Ultrasonic reflectivity imaging in three dimensions: Exact inverse scattering solutions for plane, cylindrical, and spherical apertures," *IEEE Trans. Biomed. Eng.*, vol. BME-28, pp. 202–220, 1981.

[12] G. B. Arfken and H. J. Weber, *Mathematical Methods for Physicists*. San Diego, CA: Academic, 1995.

[13] A. C. Tam, "Application of photoacoustic sensing techniques," *Rev. Mod. Phys.*, vol. 58, pp. 381–431, 1986.

[14] P. M. Morse and H. Feshbach, *Methods of Theoretical Physics*. New York: McGraw-Hill, 1953.

[15] Y. Xu, D. Feng, and L. V. Wang, "Exact frequency-domain reconstruction for thermoacoustic tomography: I. Planar geometry," *IEEE Trans. Med. Imag.*, vol. 21, pp. 823–828, July 2002.

[16] Y. Xu, M. H. Xu, and L. V. Wang, "Exact frequency-domain reconstruction for thermoacoustic tomography: II. Cylindrical geometry," *IEEE Trans.. Med. Imag.*, vol. 21, pp. 829–833, July 2002.